AGU
American Geophysical Union

Dear Author:

Thank you for publishing with AGU. Your proofs are attached. Following the annotation guidelines and returning the proofs quickly will allow prompt online posting of the final version of your paper. Please note that revised proofs are sent only in the case of extensive corrections upon author request.

We have added several new features to the journal Websites and additional services that we want to bring to your attention. The online version of your paper is enhanced in several ways, and will now include "altmetrics," which continually tracks and links to mentions in news outlets, twitter, blogs, and other social media. A link to scholarly citations is also provided. Papers are also available in a regular PDF and as a ReadCube version, which includes the altmetrics information and dynamic links to references and figures.

Please follow our social media sites! Several of our journals have social media sites; these and other AGU sites are indexed here.

If you have not already, we encourage you to create an ORCID (Open Researcher and Contributor ID) so that your work can be uniquely tracked. Your ORCID can be created and linked through your GEMS account.

Finally, your feedback is important to us. If you have questions or comments regarding your AGU Publications experience, including information on production and proofs, please contact us at publications@agu.org. For questions specific to this paper, please contact the production editor at GRLprod@wiley.com. We will also be contacting you soon after your article is published with an author survey. Please take a few minutes to respond to this online survey; your input is important in improving the overall editorial and production process.

Thank you again for supporting AGU.

Sincerely,

Brooks Hanson
Director, Publications AGU
bhanson@agu.org

2000 Florida Avenue, NW, Washington, DC 20009-1277
Tel: 202.462.6900
Fax: +1 202.328.0566
www.agu.org

PLEASE COMPLETE THE PUBLICATION FEE CONSENT FORM BELOW
AND
RETURN TO THE PRODUCTION EDITOR WITH YOUR PROOF CORRECTIONS

Please return this completed form and direct any questions to the Wiley Journal Production Editor at GRLprod@wiley.com.

To order OnlineOpen, you must complete the OnlineOpen order form at:
https://authorservices.wiley.com/bauthor/onlineopen_order.asp
Authors who select OnlineOpen will be charged the standard OnlineOpen fee for your journal, but excess publication fees will still apply, if applicable. **If your paper has generated excess publication fees, please complete and return the form below in addition to completing the OnlineOpen order form online (excess fees are billed separately)**. If you would like to choose OnlineOpen and you have not already submitted your order online, please do so now.

YOUR ARTICLE DETAILS

Journal: *Geophysical Research Letters*
Article: Jiang, H., G. Feng, T. Wang, and R. Bürgmann (2017), Toward full exploitation of coherent and incoherent information in Sentinel-1 TOPS data for retrieving surface displacement: Application to the 2016 Kumamoto (Japan) earthquake, *Geophys. Res. Lett.*, 44, doi:10.1002/2016GL072253.

OnlineOpen: No   **Words:** 4,749   **Tables:** 0   **Figures:** 3   **Total Publishing Units:** 12

Journal Base Fee: $500
Excess Publishing Units: 0@$125 $0
Publication Fee Total: USD $500

Please provide the information requested below.
Bill to:

Name: _____

Institution: _____

Address: _____

Phone: _____   **Email:** _____

Signature: _____   **Date:** _____

An invoice will be mailed to the address you have provided once your edited article publishes online in its final format. Please include on this publication fee form any information that must be included on the invoice.

Publication Fees and Length Guidelines:
http://publications.agu.org/author-resource-center/

Frequently Asked Billing Questions:
http://onlinelibrary.wiley.com/journal/10.1002/(ISSN)2169-8996/homepage/billing_faqs.pdf

Purchase Order Instructions:
Wiley must be listed as the contractor on purchase orders to prevent delay in processing invoices and payments.

AGU PUBLICATIONS

Geophysical Research Letters

RESEARCH LETTER

Key Points:
- Methods to fully exploit Sentinel-1 TOPS images for large displacement
- Improved near-field coseismic displacements of the Kumamoto earthquake
- More shallow slip after adding near-field constraints

Supporting Information:
- Supporting Information S1

Correspondence to:
T. Wang,
wang.teng@gmail.com

Toward full exploitation of coherent and incoherent information in Sentinel-1 TOPS data for retrieving surface displacement: Application to the 2016 Kumamoto (Japan) earthquake

Houjun Jiang[1] iD **, Guangcai Feng[2], Teng Wang[3,4]** iD **, and Roland Bürgmann[5]** iD

[1]Department of Surveying and Geoinformatics, Nanjing University of Posts and Telecommunications, Nanjing, China, [2]Laboratory of Radar Remote Sensing, School of Geosciences and Info-Physics, Central South University, Changsha, China, [3]Huffington Department of Earth Sciences, Southern Methodist University, Dallas, Texas, USA, [4]Now at Earth Observatory of Singapore, Nanyang Technological University, Nanyang Ave, Singapore, [5]Department of Earth and Planetary Science, University of California, Berkeley, California, USA

Abstract Sentinel-1's continuous observation program over all major plate boundary regions makes it well suited for earthquake studies. However, decorrelation due to large displacement gradients and limited azimuth resolution of the Terrain Observation by Progressive Scan (TOPS) data challenge acquiring measurements in the near field of many earthquake ruptures and prevent measurements of displacements in the along-track direction. Here we propose to fully exploit the coherent and incoherent information of TOPS data by using standard interferometric synthetic aperture radar (InSAR), split-bandwidth interferometry in range and azimuth, swath/burst-overlap interferometry, and amplitude cross correlation to map displacements in both the line-of-sight and the along-track directions. Application to the 2016 Kumamoto earthquake sequence reveals the coseismic displacements from the far field to the near field. By adding near-field constraints, the derived slip model reveals more shallow slip than obtained when only using far-field data from InSAR, highlighting the importance of exploiting all coherent and incoherent information in TOPS data.

1. Introduction

The launches of European Space Agency's (ESA's) Sentinel-1A on 3 April 2014 and Sentinel-1B on 16 April 2016 started a new era of operational interferometric synthetic aperture radar (InSAR) observations on a continental scale with down to 6 day repeat times. The large data coverage and ESA's open-data policy make Sentinel-1A/B an important data source to study surface displacements resulting from tectonic and volcanic activities, such as the 2014–2015 Fogo volcano eruption [*González et al.*, 2015], the 2015 Gorkha (Nepal) earthquake [*Avouac et al.*, 2015; *Elliott et al.*, 2016], the 2015 Illapel (Chile) earthquake [*Grandin et al.*, 2016], the 2015 Wolf (Galápagos) eruption [*Xu et al.*, 2016a], and more recent events. The general availability of recent pre-event acquisitions in active plate boundary zones and short repeat cycle of Sentinel-1 benefit from the 250 km wide ground track of the SAR images. However, such advantages are at the expense of resolution loss in the azimuth direction (satellite flying direction) due to the Terrain Observation by Progressive Scan (TOPS) technique, which decreases the illuminating time of ground targets during the data acquisition [*De Zan and Guarnieri*, 2006]. Consequently, the image resolution in azimuth has been reduced from about 5 m of previous ESA missions such as ERS and Envisat, to about 20 m for Sentinel-1 TOPS data, despite that the ground range resolution is improved from ~20 m to ~5 m for compensation. Another drawback of using Sentinel-1 data is the relatively short wavelength of the C-band, which often causes phase aliasing and absence of measurement in strongly deformed areas near earthquake ruptures and volcanoes. Meanwhile, recent studies have pointed to the importance of near-field constraints in coseismic slip model inversions, as such data provide crucial information on the complex geometry and slip of ruptures in the upper few km of the crust [e.g., *Wang et al.*, 2015; *Milliner et al.*, 2016; *Vallage et al.*, 2015; *Xu et al.*, 2016b].

SAR images contain coherent (interferometric phases) and incoherent (amplitude features) information. From the coherent information, standard InSAR can provide the most accurate displacement measurement in the line-of-sight (LOS) direction, if the corresponding interferogram can be correctly unwrapped. Taking advantage of the spectral diversity of SAR images, split-bandwidth interferometry can estimate pixel shifts

between two images in both azimuth and range directions [*Scheiber and Moreira*, 2000]. This technique has been widely used for improving SAR image coregistration and has been used for estimating surface displacements in the azimuth direction, also referred to as Multiple-Aperture Interferometry (MAI) [e.g., *Bechor and Zebker*, 2006; *Jung et al.*, 2009]. Although the reduced resolution of TOPS data seriously degrades the feasibility of MAI [*Jung et al.*, 2013], the burst- and swath-overlap area can be used to retrieve motions along the azimuth direction with remarkable accuracy, thanks to the large (maximum 1°) squint angle differences between adjacent bursts and swaths [e.g., *Grandin et al.*, 2016; *Fattahi et al.*, 2016]. In contrast to the widely applied MAI technique, split-bandwidth interferometry in range has not previously been used for retrieving surface displacements because it measures the displacement in the same direction as standard InSAR, yet with much less accuracy.

Although standard InSAR is generally the first choice to retrieve the ground displacement, phase is recorded modulo 2π and therefore must be unwrapped to provide meaningful measurements. For smooth displacement fields, most algorithms can successfully unwrap interferograms under the assumption that the absolute values of the true phase differences between adjacent pixels are less than half a cycle. However, the half-cycle assumption can be violated in areas where high-gradient displacements occur, such as near large/shallow earthquake ruptures, where split-bandwidth interferometry in range can be applied to provide LOS displacement measurement instead of InSAR. However, phase unwrapping can also be problematic for the split-bandwidth interferometry where ruptures reach the surface and cause multimeter displacement discontinuities. For such cases, it is difficult to correctly estimate the number of cycles across phase discontinuities only from wrapped phases. As ground displacements can also be estimated from cross-correlating amplitude subimages, i.e., by exploiting the incoherent information in SAR images [e.g., *Wang and Jónsson*, 2015; *Wang et al.*, 2015], we can use this information to help unwrap standard and split-bandwidth interferograms. While pixel offsets estimated from amplitude images are less precise than the InSAR and split-bandwidth interferometry observations [*De Zan*, 2014], they can provide unambiguous ground displacements very close to the area with largest strain, where interferometric phases cannot be resolved.

Here we report on fully exploiting coherent and incoherent information in the Sentinel-1 TOPS SAR images to measure the coseismic displacements of the recent 2016 Kumamoto (Japan) earthquake sequence by using standard InSAR, split-bandwidth interferometry, burst/swath-overlap interferometry, and amplitude cross correlation. InSAR provides the most accurate results in the far field but is completely decorrelated near the surface rupture. For the first time, the split-bandwidth interferometry in range is applied to reveal the near-field LOS displacement. The unwrapping of the split-bandwidth interferogram is facilitated by pixel offsets derived from amplitude cross correlation. We also map the displacement in the azimuth direction along the 1.5 km wide burst-overlap and the 2.5 km wide swath-overlap areas. Adding near-field and azimuth constraints increases the resolution of the slip distribution, particularly in the shallow part of the crust, implying that it is essential to take advantage of all the coherent and incoherent information in the Sentinel-1 TOPS data for studying geodynamic processes that produce large displacements.

2. Fully Exploit Coherent and Incoherent Information From Sentinel-1 TOPS Data

2.1. Terrain Observation by Progressive Scan (TOPS) Imaging Technique

To fulfill the requirements of large coverage and short repeat cycle, the TOPS technique is utilized for Sentinel-1's main operational imaging mode—the interferometric wide swath mode (IW) (Figure 1a) [*Torres et al.*, 2012]. In the IW mode, SAR acquires three adjacent subswaths, covering a 250 km wide ground range by periodically switching the antenna beam in elevation (Figure 1a). Each subswath is imaged in consecutive bursts that span an area that is ~85 km wide and ~20 km long. The ~1.5 km overlap in the azimuth direction between consecutive bursts ensures that all the subswaths are imaged without any gap. The IW mode illuminates the ground in a similar way as the ScanSAR imaging mode, but the latter acquires the burst image with a fixed squint angle and observes ground targets from different portions of the antenna beam in azimuth. Therefore, the antenna gain for each target varies along azimuth, causing a quality degradation of ScanSAR data, such as a periodic modulation of image amplitude (scalloping), and an azimuth-varying resolution and signal-to-noise ratio (SNR). TOPS overcomes this drawback by rotating the antenna beam from backward to forward during the burst acquisition (Figure 1a). Consequently, the sensor observes all ground targets with the complete azimuth antenna pattern, dramatically reducing the variation of image quality
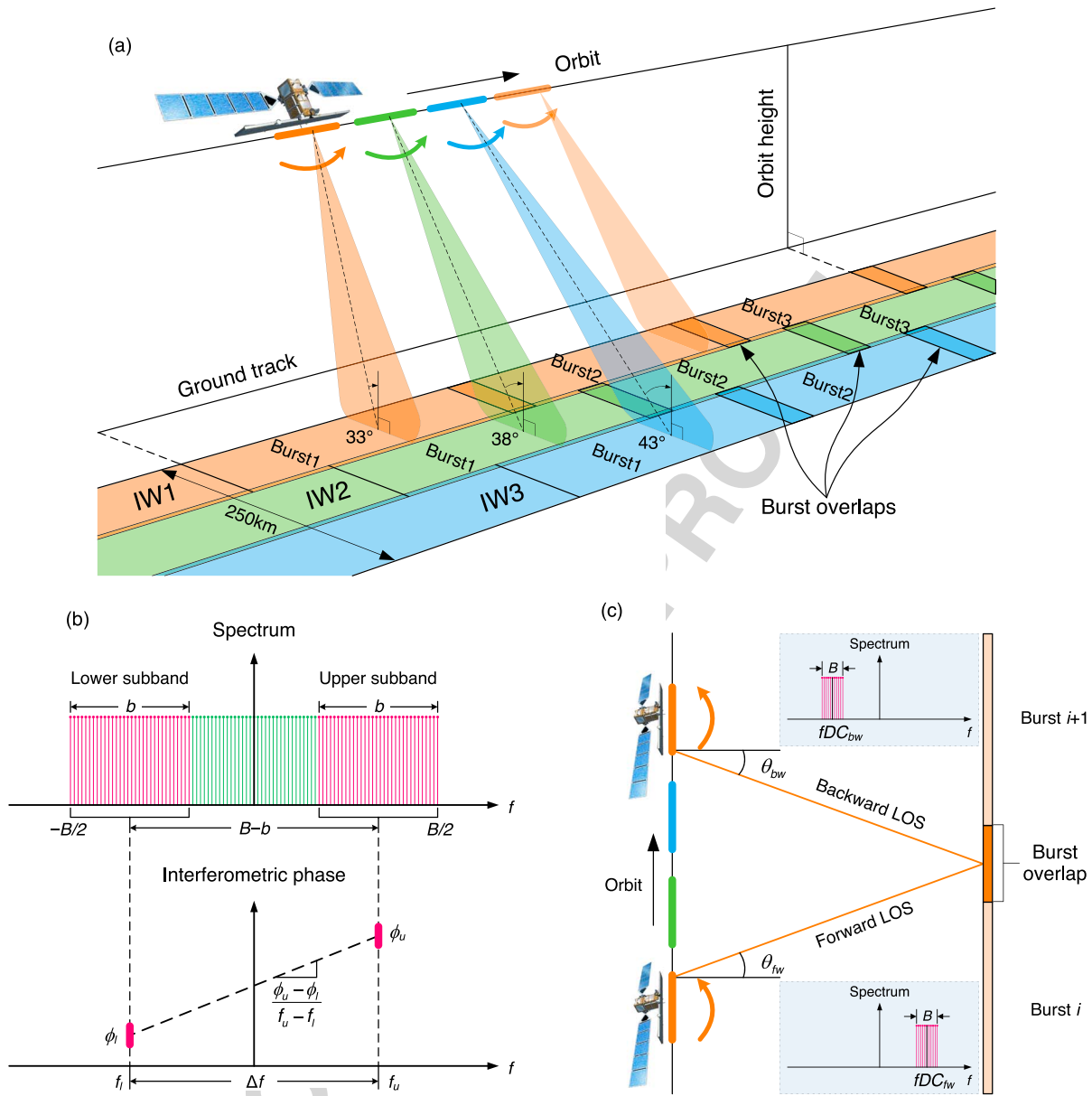
Figure 1. (a) Sentinel-1 TOPS acquisition geometry and (b) the principle of split-bandwidth and (c) burst-overlap interferometries. The split-bandwidth operation and the corresponding phase slope between a lower and an upper sub-band are shown in Figure 1b. The imaging geometry of TOPS burst overlap is shown in Figure 1c.

along the azimuth direction. Thanks to the electronic scanning capability of modern spaceborne SAR and recent progress in orbitography, TOPS that operates in nearly perfect scan synchronization, i.e., with sufficient azimuth spectral overlap for interferometry, can be implemented without a complete redesign of existing SAR systems, making it a superior, and probably the only choice until the onboard implementation of advanced multichannel SAR systems that can acquire high-resolution wide-swath SAR images [e.g., *Krieger et al.*, 2010].

In comparison with its predecessors, Sentinel-1 achieves an approximately threefold improvement in slant-range resolution (from ~10 m of ERS/Envisat to ~3 m) because of the notable increase of range bandwidth from 16 MHz to 49 MHz. Meanwhile, because the illuminated area is almost 3 times wider, the minimum repeat cycle of Sentinel-1A has also been reduced from 35 days of ERS/Envisat to 12 days, and it has been shortened to 6 days since the launch of the twin satellite Sentinel-1B. The higher resolution in range and the shorter repeat cycle can better preserve the phase coherence and speckle pattern between two

acquisitions, providing high SNR for both interferometry and offset tracking. However, the Sentinel-1 mission's large coverage is achieved at the expense of reduced azimuth bandwidth, and consequently lower azimuth resolution, preventing the retrieval of small displacements in the azimuth direction.

2.2. Split-Bandwidth Interferometry for TOPS Data

It is difficult for standard InSAR to acquire reliable measurements in the near field if the displacement gradients are large. For such cases, we can estimate ground displacements from the phase difference between interferograms of different spectral looks, i.e., split-bandwidth interferometry [e.g., *Scheiber and Moreira*, 2000; *Bamler and Eineder*, 2005; *Bechor and Zebker*, 2006; *Barbot et al.*, 2008; *Jung et al.*, 2009]. This method is based on the fact that phase differences between interferograms formed by using lower and upper portions of imaging spectrum reflect pixel shifts between two SAR images. As the impulse response of a SAR system has a phase ramp depending on the signal's center frequency f_c (Figure 1b), given a pixel offset Δt in seconds, the phase ramp will lead to an additional phase term $2\pi f_c \Delta t$ in standard InSAR, added to the phase containing topography, atmospheric delay, and displacement. We can extract the pixel shift by performing a phase differential operation between two interferograms from the same image pair with different azimuth or range center frequencies but identical interferometric phases. After that, we can convert the pixel shift Δt to displacement by multiplying with the image sampling frequency and pixel spacing.

Thanks to the large bandwidth in modern SAR systems, we can split a pair of SAR images m and s into four low-resolution sublook images m_l, m_u, s_l, and s_u by filtering out the lower and upper bands in the frequency domain (Figure 1b). Then, two interferograms are formed by combining the sublook images with common spectra. The phase difference ϕ_{split} of the two interferograms can be derived from $(m_u \cdot s_u^*) \cdot (m_l \cdot s_l^*)^*$, where the asterisk indicates conjugate multiplication. Finally, we can retrieve the pixel shift Δt in units of time from the phase differences between the two sublook interferograms because the phase differences correspond to $2\pi \Delta f_c \Delta t$, given the spectral separation Δf_c of the sublook images [*Scheiber and Moreira*, 2000]:

$$\Delta t = \frac{\phi_u - \phi_l}{2\pi (f_{c,u} - f_{c,l})} = \frac{\phi_{\text{split}}}{2\pi \Delta f_c} \tag{1}$$

Note that in range split-bandwidth interferometry, the phase difference ϕ_{split} contains a component corresponding to the pixel shift produced by topography and InSAR baseline. This component should be removed by using orbit ephemerides and an external digital elevation model (DEM) during the DEM-assisted coregistration [e.g., *Sansosti et al.*, 2000; *Wang et al.*, 2014]. In the azimuth component, little topographic information remains in ϕ_{split} because the azimuth offsets are insensitive to the cross-track baseline. Note that the ionospheric delay can also introduce ionospheric phase screen in the circumstances of significantly variation of ionospheric conditions between acquisitions [e.g., *Gomba et al.*, 2016]. Although ionospheric effects are relatively small at C band, split-bandwidth interferograms must be carefully examined before converting to displacement.

For TOPS data, a larger spectral separation of range sublooks can be achieved compared to previous ESA satellites, dramatically improving the sensitivity and accuracy of range split-bandwidth interferometry. However, to the best knowledge of the authors, range split-bandwidth interferometry has not been applied in previous earthquake studies by using Sentinel-1 TOPS data. In the azimuth direction, due to the reduced bandwidth, the accuracy of azimuth split-bandwidth interferometry is decreased for TOPS data. However, we can map along-track displacement with a much higher accuracy in the burst-overlap area than within each burst. This is because the sensor observes ground targets in the burst-overlap area twice from different squint angles (i.e., different Doppler centroid frequencies) due to the azimuth steering of the antenna beam (Figure 1c). We can directly obtain the phase difference ϕ_{split} of pixels in each burst overlap from $(m_i \cdot s_i^*) \cdot (m_{i+1} \cdot s_{i+1}^*)^*$. Since the difference in Doppler centroid frequency (~4300 Hz) is much larger than the spectral separation available from the processed azimuth bandwidth (~310 Hz), the azimuth split-bandwidth interferometry is much more sensitive to the along-track displacement in the burst overlap area. Similarly, there is also useful information in the swath-overlap areas, where the difference in Doppler centroid frequency is one third of that in the burst-overlap area. According to equation (1), the corresponding sensitivities to ground displacements for one cycle of ϕ_{split} are ~4.6 m, ~32 m, ~1.6 m, and ~5 m, for range, azimuth,

burst-overlap interferometry, and swath-overlap split-bandwidth interferometry, respectively. As for measuring along-track displacements, the burst- and swath-overlap interferometries are ~20 times and ~6 times more sensitive than MAI, but measurements are only available along burst and swath overlapping areas [e.g., *Grandin et al.*, 2016].

Although the coherent cross correlation is the maximum likelihood estimator for the pixel offset between distributed Gaussian targets, the requirement of removing interferometric phase complicates its implementation. Therefore, split-bandwidth interferometry is often used in practice with accuracy determined by the interferometric coherence γ and the spectral separation Δf_c. In theory, the standard deviations in displacement estimation from the split-bandwidth interferometry are given by [*Bamler and Eineder*, 2005]:

$$\sigma = \frac{1}{2\pi\Delta f_c} \frac{1}{\sqrt{N}} \sqrt{\frac{B}{b}} \frac{\sqrt{1-\gamma^2}}{\gamma} \frac{p_{\text{spa}}}{\Delta t_s} \qquad (2)$$

where $\Delta f_c = B - b$, B is the processed bandwidth of a single target, b is the sublook bandwidth which is often selected to be a third of the bandwidth [*De Zan*, 2011; *Bamler and Eineder*, 2005], N is the number of independent samples averaged, Δt_s is the image sampling in seconds, and p_{spa} is the pixel spacing. For the burst overlap area, $B = b$ and $\Delta f_c = \Delta f_{\text{DC}}$, which is the Doppler centroid frequency difference between adjacent bursts. For Sentinel-1 TOPS data, B is 49 MHz in range and 310 Hz in azimuth and Δf_{DC} is 4300 Hz. If we assume $\gamma = 0.4$, then $N = 900$ (300 × 300 m posting) and $b = B/3$, σ is ~0.1 m in range direction and is ~0.7 m in azimuth direction for split-bandwidth interferometry, and σ is ~0.02 m in the burst-overlap area and ~0.06 m in the swath-overlap area. Due to the reduced sensitivity to displacement gradient, split-bandwidth interferometry also allows for more multilooking than is possible with standard interferometric phase in highly deformed areas, further improving the accuracy in low coherence areas.

2.3. Amplitude Cross-Correlation for Displacement Discontinuity

Each interferometric fringe of Sentinel-1 TOPS data represents only about 28 mm displacement difference, often causing phase aliasing in the near field where the displacement gradient is large. Phase unwrapping errors are likely and consequently can bias the geophysical model inversion. This is even the case for split-bandwidth interferometry when the rupture reaches the surface, producing a multimeter displacement discontinuity. We need auxiliary information such as field observations to determine the exact trace of the rupture to avoid the unwrapping path going through the discontinuity. Such field observations are often hard to obtain and rarely dense enough to determine the complete trace. On the other hand, large displacements can be measured from the shift of small image patches distributed in the SAR images spanning the event, by searching for the peaks of an oversampled correlation surface calculated between them [*Michel et al.*, 1999; *Wang and Jónsson*, 2015]. This technique can estimate ground deformation in both range and azimuth directions with the precision of a small fraction (~5%) of the size of resolution cell.

Pixel offsets from amplitude cross correlation allow for determining the displacement discontinuities regardless of the phase coherence because the offsets are estimated from amplitude features [e.g., *Wang et al.*, 2015]. Then the determined rupture trace can be used to assist the phase unwrapping of the interferograms. Thus, we can fully utilize the coherent and incoherent information in Sentinel-1 TOPS data for retrieving the 2-D ground displacement field, from the far field to the near field by using standard interferometry, split-bandwidth interferometry, burst/swath-overlap interferometry, and amplitude cross correlation. Thanks to Sentinel-1A/B's dense footprints along plate boundaries, images from ascending and descending tracks are often available, allowing for resolving 3-D motions when the NS motion can be interpolated from the azimuth displacements measured in burst-overlap areas [e.g., *Grandin et al.*, 2016], or they can be measured from SAR images acquired by other satellites or from cross-correlating optical images, e.g., Sentinel-2 data.

3. Application to the 2016 Kumamoto Earthquake

3.1. Coseismic Displacement Derived From Sentinel-1 TOPS Data

The 2016 Kumamoto earthquake sequence struck south Japan beneath Kyushu Island, causing 72 fatalities, more than 1000 injuries, and widespread destruction [e.g., *Lin et al.*, 2016]. The sequence began with two
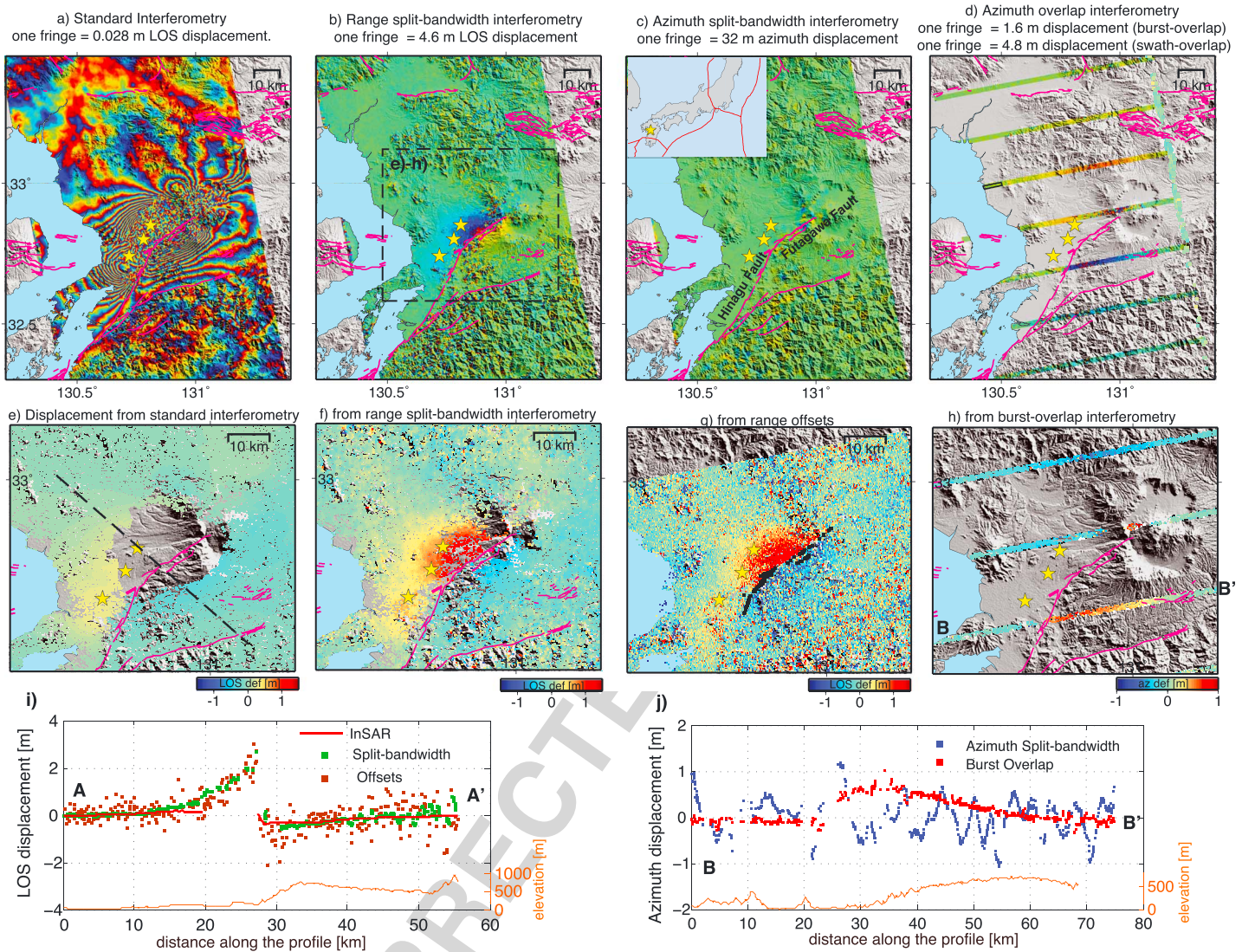
Figure 2. Coseismic displacements of the 2016 Kumamoto earthquake sequence mapped from the ascending Sentinel-1 TOPS data, using (a and e) InSAR, (b and f) split-bandwidth interferometry in range and in (c) azimuth, (g) range offsets from amplitude cross correlation, and (d and h) burst- and swath-overlap interferometries. The earthquake locations (yellow stars) are from global CMT. The mapped faults are indicated as magenta lines. The black dots in Figure 2g are filed observations of surface rupture [*Shirahama et al.*, 2016]. The color scales plotted at the bottom right of Figure 2e–2h are for the derived displacements of the unwrapped interferograms and range offsets. The line-of-sight (LOS) displacement measured by using InSAR, split-bandwidth interferometry, and amplitude cross correlation is compared along the (i) profile AA'. The along-track displacement measured by using split-bandwidth interferometry in azimuth and burst-overlap interferometry is compared along the (j) profile BB'.

strong foreshocks on 14 and 15 April, respectively, and the main shock occurred on 16 April near the two foreshocks (Figure 2). The sequence ruptured the Hinagu and Futagawa faults, which represent the main active intraplate fault zone on Kyushu Island of Japan [*Lin et al.*, 2016]. These faults make up the westernmost section of the Median Tectonic Line that accommodates right-lateral motion within the island arc of the Nankai subduction zone. Previous InSAR studies of the event using ALOS-2 interferometry show that, in addition to the primary surface rupture, a multitude of smaller faults experienced small offsets across the wider epicentral region [*Fujiwara et al.*, 2016].

Two Sentinel-1A tracks (ascending tracks AT156 and descending track DT163) covering the entire epicentral area were processed by using our TOPS data processing package (see the supporting information for details). Both preseismic images were acquired on 8 April and both postseismic images were acquired on 20 April; the time period of the interferograms includes the four $M > 5.5$ foreshocks and 4 days of postseismic motion. Due
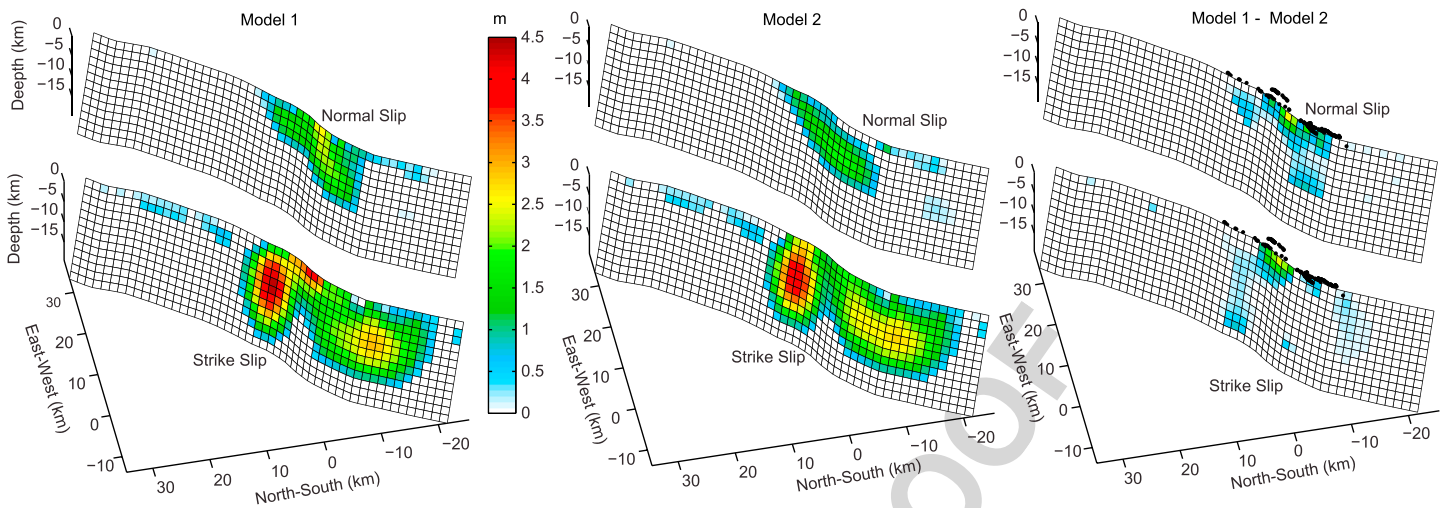
Figure 3. Slip distribution estimated from the Sentinel-1 TOPS data. (a) Model 1 is derived from InSAR plus near-field constraints from split-bandwidth interferometry in range, burst-overlap interferometry in azimuth, and range offsets from amplitude cross correlation. (b) Model 2 is derived from InSAR only. (c) Their differences are shown with black dots indicating field observations of surface rupture [*Shirahama et al.*, 2016].

to the fault orientation, SAR acquisition geometry, and coherence levels, the results from the ascending track exhibit clearer signal along the rupture, which are shown here (Figure 2).

The improvement of using range split-bandwidth interferometry, instead of standard InSAR, is clearly visible in the near field along the rupture (Figures 2a and 2b). The observed sharp phase discontinuity obtained from split-bandwidth and burst-overlap interferograms consistently follows the mapped fault in this region (Figures 2b and 2d). By using the range split-bandwidth interferometry, we are able to extend high-quality displacement measurements from the far field to the rupture trace, while the unwrapped standard InSAR interferogram may underestimate the surface displacement due to phase aliasing and decorrelation. Such underestimation of displacement due to incorrect phase unwrapping and/or lack of constrain in the near field have also been noted in a recent study about the apparent shallow slip deficit of many large strike-slip earthquakes [*Xu et al.*, 2016b]. Nevertheless, there are still some segments along the rupture with a displacement difference larger than 2.3 m, half of the phase-to-displacement ratio of split-bandwidth interferometry in range. Here we have to prevent unwrapping across the displacement discontinuity by setting a cut line derived from the amplitude offsets, consistent with field observations of the primary surface rupture [*Shirahama et al.*, 2016]. By doing this, we can correctly unwrap the split-bandwidth interferogram without crossing the rupture and obtain the displacements in the LOS direction.

The standard deviations of displacements estimated from the coherent information (four interferograms, Figures 2a–2d; we exclude the swath-overlap interferogram as it is too far from the ruptures) and incoherent information (range offsets, Figure 2g) were calculated within a burst-overlap area about 40 km away from the epicenter (black rectangle in Figure 2d). These error estimates are 3.9 mm for InSAR, 176.1 mm and 42.9 mm for azimuth and range split-bandwidth interferometry, 25.1 mm for the burst-overlap interferometry, and 213.8 mm for the range offsets. The values from the split-bandwidth interferometry are smaller than the theoretical calculation provided above because of higher coherence in the urban area. Moreover, all split-bandwidth interferograms are Goldstein filtered [*Goldstein and Werner*, 1998], while the burst-overlap interferogram and range offsets are not filtered, resulting in higher standard deviations. The large value from range offsets is also partly due to the remaining outliers and partly due to relatively less samples used for the accuracy evaluation.

3.2. The Slip Distribution From Sentinel-1 TOPS Data

To highlight the improved observation in the near field, we use a first-order model to explore the slip distribution of the Kumamoto earthquake with a focus resolving the shallow slip (see Text S1 and Figure S1 in the supporting information for data downsampling and slip inversion methods). We neglect slip on secondary

fault strands and vertical and lateral variations in elastic material properties and only use the two tracks of Sentinel-1 data, not the extensive additional constraints from other SAR satellites, field observations, GPS, and seismic data [e.g., *Asano and Iwata*, 2016; *Fujiwara et al.*, 2016; *Kubo et al.*, 2016; *Lin et al.*, 2016; *Shirahama et al.*, 2016; *Yoshida et al.*, 2016].

Two slip models were calculated with (Model 1) and without (Model 2) using the near-field data in the inversion. Both models show that the dominant mechanism is right-lateral strike slip with a component of normal faulting, with a dip angle of 73° to the northwest (Figure 3), consistent with main shock and foreshock focal **F3** mechanisms, the distribution of aftershocks, and field measurements [*Asano and Iwata*, 2016; *Lin et al.*, 2016; *Uchide et al.*, 2016]. Two models also show similar slip distribution along the main rupture except for both the strike and dip slip in the shallow middle part of the fault plane, where Model 1 has much larger slip than Model 2 near the surface (Figure 3). The larger shallow slip of Model 1 is independently supported by the field observations of *Shirahama et al.* [2016], showing that most of the observable surface rupture occurred at locations only Model 1 has or Model 1 has larger slips than Model 2 (Figure 3c). Our models predict maximum values of 4.5 m of right-lateral slip and 2.5 m of normal slip at depth, suggesting that the slip is concentrated in the upper crust, with maximum values at 10 km depth. We find that the normal component of slip is mostly limited to the upper 10 km and has a more concentrated distribution along a releasing bend of the Hinagu-Futagawa fault zone, in comparison with the extent of the right-lateral slip. The geodetic moments of Models 1 and 2 are very close to each other, corresponding to an M_w 7.02 earthquake. Note that the displacement we captured includes also four $M > 5$ preshocks and 4 days of postseismic motion, which explains the obtained higher magnitude.

4. Discussion and Conclusions

Since the Sentinel-1 TOPS data have been introduced to the geophysical community, arguments about the burst-based acquisition mode, reduced azimuth resolution, and additional processing steps have been widespread. Nevertheless, the benefit of using this acquisition mode has been demonstrated by the fact that surface displacements resulting from almost all recent tectonic and volcanic events have been well captured by Sentinel-1A/B TOPS images. This would not have been possible if the traditional strip-map acquisition mode with its more limited acquisition schedule was used. However, near the rupture surface, decorrelation of standard InSAR and the low SNR of amplitude offsets limit the resolution of imaging the shallow slip in geophysical models. Our study shows that, when the loss of coherence is mainly due to the large displacement, split-bandwidth interferometry can be implemented to retrieve near-field deformation in the range direction instead of standard InSAR, thanks to the improved range bandwidth of TOPS data. We still take advantage of estimating the pixel offsets from amplitude features along the displacement discontinuity where neither InSAR nor split-bandwidth interferometry can provide reliable estimation of the displacement across the fault if it is large.

The 2016 Kumamoto earthquake sequence ruptured the shallow crust up to the surface near a highly populated urban region. This event is an ideal case for implementing the split-bandwidth interferometry to fill the missing part from standard InSAR in the near field. The retrieved displacements near the rupture are important to improve the slip resolution of the shallow parts of the fault plane. Interestingly, clear north-south displacement can be identified from burst-overlap interferometry not only along the known Futagawa fault but also extending further north (Figure 2d), implying complex fault structure beneath Kyushu island.

The proposed methods and application are the first attempt of overcoming the decorrelation and unwrapping limitations of Sentinel-1 TOPS data by applying split-bandwidth interferometry in range. Pixel offsets identify the rupture trace and facilitate unwrapping, extending the measurements up to the ground ruptures. The burst-overlap interferometry can partially make up for the limited azimuth-offset resolution by acquiring accurate displacement measurements along the 1.5 km wide bands spaced 20 km apart, providing additional constraints for the slip distribution. Note that the proposed methods (except for the burst/swath-overlap interferometry) are applicable for images acquired from all SAR missions, allowing for overcoming the azimuth limitation of Sentinel-1 data. However, Sentinel-1 TOPS data are still often the first choice once an earthquake occurs because of their frequent and comprehensive acquisitions and open data policy. The application to the recent Kumamoto earthquake sequence demonstrates the capability of the proposed methods for extending the interferometric measurements to the rupture trace. The derived slip

distribution model exhibits higher resolution in the shallow part, as shown in the differences between the two models (Figure 3), benefitting from the additional constraints in the near field. We should therefore take advantage of all the coherent and incoherent information in Sentinel-1 TOPS data for retrieving both near- and far-field surface displacements produced from many geodynamic processes.

References

Asano, K., and T. Iwata (2016), Source rupture processes of the foreshock and mainshock in the 2016 Kumamoto earthquake sequence estimated from the kinematic waveform inversion of strong motion data, *Earth Planets Space*, 68(1), 147, doi:10.1186/s40623-016-0519-9.

Avouac, J.-P., L. Meng, S. Wei, T. Wang, and J.-P. Ampuero (2015), Lower edge of locked Main Himalayan Thrust unzipped by the 2015 Gorkha earthquake, *Nat. Geosci.*, doi:10.1038/ngeo2518.

Bamler, R., and M. Eineder (2005), Accuracy of differential shift estimation by correlation and split-bandwidth interferometry for wideband and delta-k SAR systems, *IEEE Geosci. Remote Sens. Lett.*, 2(2), 151–155.

Barbot, S., Y. Hamiel, and Y. Fialko (2008), Space geodetic investigation of the coseismic and postseismic deformation due to the 2003 M_w 7.2 Altai earthquake: Implications for the local lithospheric, *J. Geophys. Res.*, 113 B03403, doi:10.1029/2007JB005063.

Bechor, N. B., and H. A. Zebker (2006), Measuring two-dimensional movements using a single InSAR pair, *Geophys. Res. Lett.*, 33 L16311, doi:10.1029/2006GL026883.

Chen, C. W., and H. A. Zebker (2001), Two-dimensional phase unwrapping with use of statistical models for cost functions in nonlinear optimization, *J. Opt. Soc. Am. A*, 18(2), 338–351.

De Zan, F. (2011), Coherent shift estimation for stacks of SAR images, *IEEE Geosci. Remote Sens. Lett.*, 8(6), 1095–1099, doi:10.1109/LGRS.2011.2157079.

De Zan, F. (2014), Accuracy of incoherent speckle tracking for circular Gaussian signals, *IEEE Geosci. Remote Sens. Lett.*, 11(1), 264–267.

De Zan, F., and A. M. Guarnieri (2006), TOPSAR: Terrain Observation by Progressive Scans, *IEEE Trans. Geosci. Remote Sens.*, doi:10.1109/TGRS.2006.873853.

Elliott, J. R., R. Jolivet, P. J. González, J.-P. Avouac, J. Hollingsworth, M. P. Searle, and V. L. Stevens (2016), Himalayan megathrust geometry and relation to topography revealed by the Gorkha earthquake, *Nat. Geosci.*, 9(2), 174–180, doi:10.1038/ngeo2623.

Fattahi, H., P. Agram, and M. Simons (2016), A network-based enhanced spectral diversity approach for TOPS time-series analysis, *IEEE Trans. Geosci. Remote Sens.*, doi:10.1109/TGRS.2016.2614925.

Fujiwara, S., et al. (2016), Small-displacement linear surface ruptures of the 2016 Kumamoto earthquake sequence detected by ALOS-2 SAR interferometry, *Earth Planets Space*, 68(1), 160, doi:10.1186/s40623-016-0534-x.

Goldstein, R. M., and C. L. Werner (1998), Radar interferogram filtering for geophysical applications, *Geophys. Res. Lett.*, 25, 4035–4038, doi:10.1029/1998GL900033.

Gomba, G., F. González, and F. De Zan (2017), Ionospheric phase screen compensation for the Sentinel-1 TOPS and ALOS-2 ScanSAR modes, *IEEE Trans. Geosci. Remote Sens.*, 55(1), 223–235.

González, P. J., M. Bagnardi, A. J. Hooper, Y. Larsen, P. Marinkovic, S. V. Samsonov, and T. J. Wright (2015), The 2014–2015 eruption of Fogo volcano: Geodetic modeling of Sentinel 1 TOPS interferometry, *Geophys. Res. Lett.*, 42, 9239–9246, doi:10.1002/2015GL066003.

Grandin, R., E. Klein, M. Métois, and C. Vigny (2016), Three-dimensional displacement field of the 2015 M_w 8.3 Illapel earthquake (Chile) from across- and along-track Sentinel-1 TOPS interferometry, *Geophys. Res. Lett.*, 43, 2552–2561, doi:10.1002/2016GL067954.

Jung, H. S., J. S. Won, and S. W. Kim (2009), An improvement of the performance of multiple-aperture SAR interferometry (MAI), *IEEE Trans. Geosci. Remote Sens.*, 47(8), 2859–2869.

Jung, H. S., Z. Lu, and L. Zhang (2013), Feasibility of along-track displacement measurement from Sentinel-1 interferometric wide-swath mode, *IEEE Trans. Geosci. Remote Sens.*, 51(1), 573–578.

Krieger, G., et al. (2012), Digital beamforming and MIMO SAR: Review and new concepts, paper presented at 9th European Conference on Synthetic Aperture Radar, EUSAR 2012, pp. 1–4, VDE, Nuremberg, Germany, 23–26 Apr.

Kubo, H., W. Suzuki, S. Aoi, and H. Sekiguchi (2016), Source rupture processes of the 2016 Kumamoto, Japan, earthquakes estimated from strong-motion waveforms, *Earth Planets Space*, 68(1), 161, doi:10.1186/s40623-016-0536-8.

Lin, A., T. Satsukawa, M. Wang, Z. Asl, R. Fueta, and F. Nakajima (2016), Coseismic rupturing stopped by Aso volcano during the 2016 M_w 7.1 Kumamoto earthquake, Japan, *Science*, doi:10.1126/science.aah4629.

Michel, R., J.-P. Avouac, and J. Taboury (1999), Measuring ground displacements from SAR amplitude images: Application to the Landers earthquake, *Geophys. Res. Lett.*, 26, 875–878, doi:10.1029/1999GL900138.

Milliner, C., C. Sammis, A. A. Allam, and J. F. Dolan (2016), Resolving fine-scale heterogeneity of co-seismic slip and the relation to fault structure, *Sci. Rep.*, doi:10.1038/srep27201.

Rucci, A., A. Ferretti, M. A. Guarnieri, and F. Rocca (2012), Sentinel 1 SAR interferometry applications: The outlook for sub millimeter measurements, *Remote Sens. Environ.*, 120, 156–163.

Sansosti, E., P. Berardino, M. Manunta, F. Serafino, and G. Fornaro (2006), Geometrical SAR image registration, *IEEE Trans. Geosci. Remote Sens.*, 44(10), 2861–2870, doi:10.1109/TGRS.2006.875787.

Scheiber, R., and A. Moreira (2000), Coregistration of interferometric SAR images using spectral diversity, *IEEE Trans. Geosci. Remote Sens.*, doi:10.1109/36.868876.

Shirahama, Y., et al. (2016), Characteristics of the surface ruptures associated with the 2016 Kumamoto earthquake sequence, central Kyushu, Japan, *Earth Planets Space*, 68(1), 191, doi:10.1186/s40623-016-0559-1.

Torres, R., et al. (2012), GMES Sentinel-1 mission, *Remote Sens. Environ.*, 120, 9–24.

Uchide, T., H. Horikawa, M. Nakai, R. Matsushita, N. Shigematsu, R. Ando, and K. Imanishi (2016), The 2016 Kumamoto-Oita earthquake sequence: Aftershock seismicity gap and dynamic triggering in volcanic areas, *Earth Planets Space*, 68(1), 180, doi:10.1186/s40623-016-0556-4.

Vallage, A., Y. Klinger, R. Grandin, and H. S. Bhat (2015), Inelastic surface deformation during the 2013 M_w 7.7 Balochistan, Pakistan, earthquake, *Geology*, doi:10.1130/G37290.1.

Wang, T., and S. Jónsson (2015), Improved SAR amplitude image offset measurements for deriving three-dimensional coseismic displacements, *IEEE J. Sel. Top. Appl. Earth Obs. Remote Sens.*, 18, doi:10.1109/JSTARS.2014.2387865.

Wang, T., S. Jónsson, and R. F. Hanssen (2014), Improved SAR image coregistration using pixel-offset series, *IEEE Geosci. Remote Sens. Lett.*, 11(9), 1465–1469.

Wang, T., S. Wei, and S. Jónsson (2015), Coseismic displacements from SAR image offsets between different satellite sensors: Application to the 2001 Bhuj (India) earthquake, *Geophys. Res. Lett.*, *42*, 7022–7030, doi:10.1002/2015GL064585.

Xu, W., S. Jónsson, J. Ruch, and Y. Aoki (2016a), The 2015 Wolf volcano (Galápagos) eruption studied using Sentinel-1 and ALOS-2 data, *Geophys. Res. Lett.*, *43*, 9573–9580, doi:10.1002/2016GL069820.

Xu, X., X. Tong, D. T. Sandwell, C. W. Milliner, J. F. Dolan, J. Hollingsworth, S. Leprince, and F. Ayoub (2016b), Refining the shallow slip deficit, *Geophys. J. Int.*, *204*(3), 1867–1886, doi:10.1093/gji/ggv563.

Yoshida, K., A. Hasegawa, T. Saito, Y. Asano, S. Tanaka, K. Sawazaki, Y. Urata, and E. Fukuyama (2016), Stress rotations due to the *M*6.5 foreshock and *M*7.3 main shock in the 2016 Kumamoto, SW Japan, earthquake sequence, *Geophys Res Lett*, *43*, 10,097–10,104, doi:10.1002/2016gl070581.

Zebker, H. A., and J. Villasenor (1992), Decorrelation in interferometric radar echoes, *IEEE Trans. Geosci. Remote Sens.*, doi:10.1109/36.175330. Q12

Author Query Form

Dear Author,

During the copyediting of your paper, the following queries arose. Please respond to these by annotating your proofs with the necessary changes/additions.
- If you intend to annotate your proof electronically, please refer to the E-annotation guidelines.
- If you intend to annotate your proof by means of hard-copy mark-up, please use the standard proofing marks. If manually writing corrections on your proof and returning it by fax, do not write too close to the edge of the paper. Please remember that illegible mark-ups may delay publication.

Whether you opt for hard-copy or electronic annotation of your proofs, we recommend that you provide additional clarification of answers to queries by entering your answers on the query sheet, in addition to the text mark-up.

| Query No.	Query	Remark
Q1	AUTHOR: Please complete the Publication Fee Consent Form included with your article and return to the Production Editor with your proofs.	
Q2	AUTHOR: Please confirm that given names (red) and surnames/family names (green) have been identified correctly.	
Q3	AUTHOR: Please check if captured affiliations are correct.	
Q4	AUTHOR: Krieger et al. (2010) does not appear in the reference list. Please add to the reference list or delete from text.	
Q5	AUTHOR: Sansosti et al. (2000) does not appear in the reference list. Please add to the reference list or delete from text.	
Q6	AUTHOR: Gomba et al. (2016) does not appear in the reference list. Please add to the reference list or delete from text.	
Q7	AUTHOR: Reference "Chen & Zebker (2001)" is not cited in the text. Please indicate where it should be cited; or delete from the reference list.	
Q8	AUTHOR: Reference "Gomba et al. (2017)" is not cited in the text. Please indicate where it should be cited; or delete from the reference list.	
Q9	AUTHOR: Reference "Krieger et al. (2012)" is not cited in the text. Please indicate where it should be cited; or delete from the reference list.	
Q10	AUTHOR: Reference "Rucci et al. (2012)" is not cited in the text. Please indicate where it should be cited; or delete from the reference list.	
Q11	AUTHOR: Reference "Sansosti et al. (2006)" is not cited in the text. Please indicate where it should be cited; or delete from the reference list.	
Q12	AUTHOR: Reference "Zebker & Villasenor (1992)" is not cited in the text. Please indicate where it should be cited; or delete from the reference list.	

USING e-ANNOTATION TOOLS FOR ELECTRONIC PROOF CORRECTION

**Required software to e-Annotate PDFs: <u>Adobe Acrobat Professional</u> or <u>Adobe Reader</u> (version 7.0 or above). (Note that this document uses screenshots from <u>Adobe Reader X</u>)
The latest version of Acrobat Reader can be downloaded for free at: <u>http://get.adobe.com/uk/reader/</u>**

Once you have Acrobat Reader open on your computer, click on the Comment tab at the right of the toolbar:
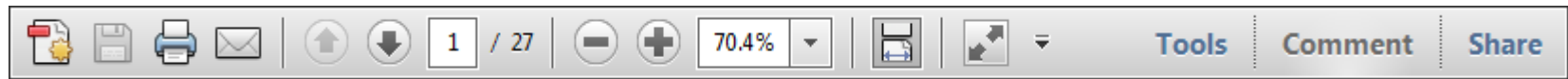
This will open up a panel down the right side of the document. The majority of tools you will use for annotating your proof will be in the Annotations section, pictured opposite. We've picked out some of these tools below:

---
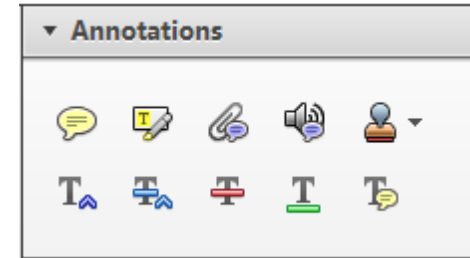
1. Replace (Ins) Tool – for replacing text.

Strikes a line through text and opens up a text box where replacement text can be entered.

How to use it

- Highlight a word or sentence.
- Click on the Replace (Ins) icon in the Annotations section.
- Type the replacement text into the blue box that appears.

---
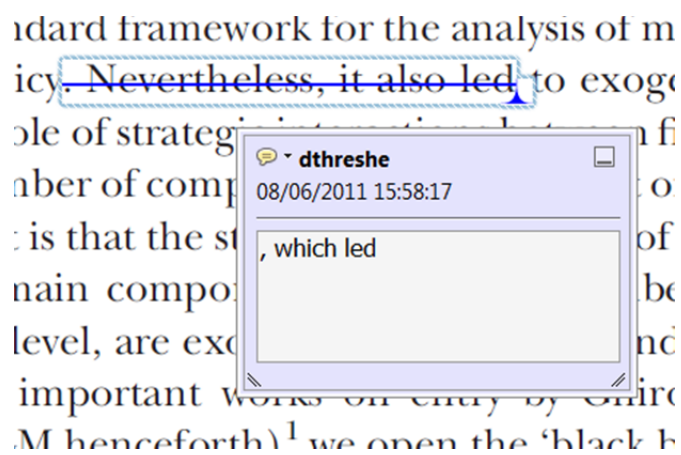
2. Strikethrough (Del) Tool – for deleting text.

Strikes a red line through text that is to be deleted.

How to use it

- Highlight a word or sentence.
- Click on the Strikethrough (Del) icon in the Annotations section.

---
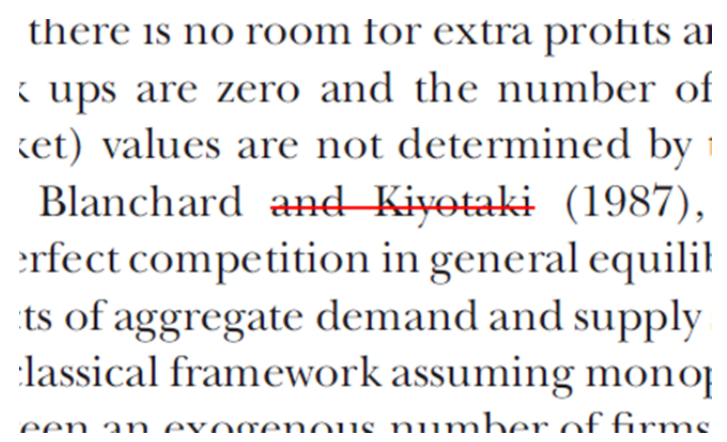
3. Add note to text Tool – for highlighting a section to be changed to bold or italic.
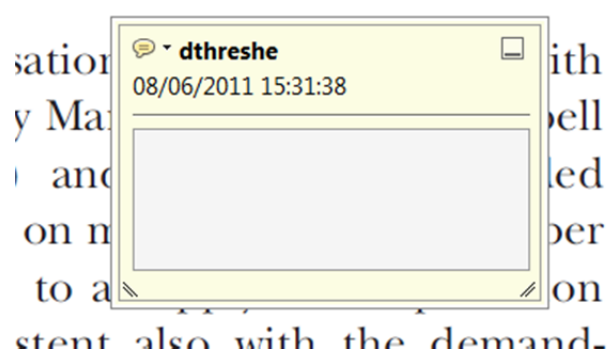
Highlights text in yellow and opens up a text box where comments can be entered.

How to use it

- Highlight the relevant section of text.
- Click on the Add note to text icon in the Annotations section.
- Type instruction on what should be changed regarding the text into the yellow box that appears.
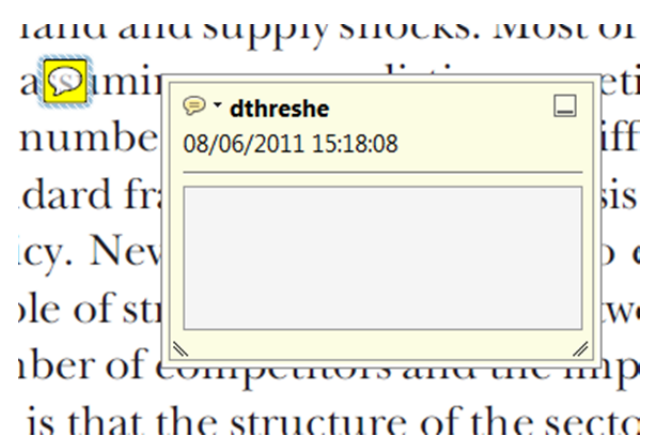

---

4. Add sticky note Tool – for making notes at specific points in the text.

Marks a point in the proof where a comment needs to be highlighted.

How to use it

- Click on the Add sticky note icon in the Annotations section.
- Click at the point in the proof where the comment should be inserted.
- Type the comment into the yellow box that appears.

5. Attach File Tool – for inserting large amounts of text or replacement figures.

Inserts an icon linking to the attached file in the appropriate pace in the text.

How to use it

- Click on the Attach File icon in the Annotations section.
- Click on the proof to where you'd like the attached file to be linked.
- Select the file to be attached from your computer or network.
- Select the colour and type of icon that will appear in the proof. Click OK.
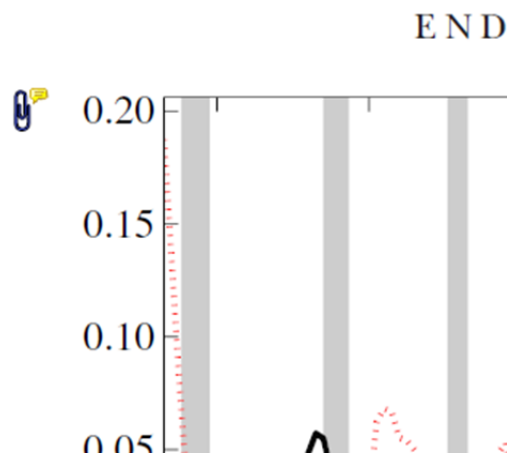
6. Add stamp Tool – for approving a proof if no corrections are required.

Inserts a selected stamp onto an appropriate place in the proof.

How to use it

- Click on the Add stamp icon in the Annotations section.
- Select the stamp you want to use. (The Approved stamp is usually available directly in the menu that appears).
- Click on the proof where you'd like the stamp to appear. (Where a proof is to be approved as it is, this would normally be on the first page).
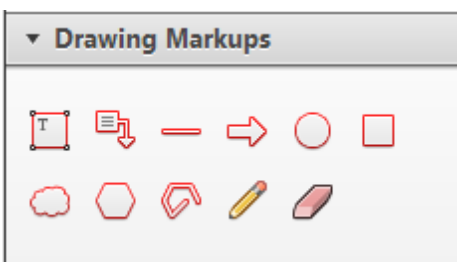
7. Drawing Markups Tools – for drawing shapes, lines and freeform annotations on proofs and commenting on these marks.

Allows shapes, lines and freeform annotations to be drawn on proofs and for comment to be made on these marks..

How to use it

- Click on one of the shapes in the Drawing Markups section.
- Click on the proof at the relevant point and draw the selected shape with the cursor.
- To add a comment to the drawn shape, move the cursor over the shape until an arrowhead appears.
- Double click on the shape and type any text in the red box that appears.
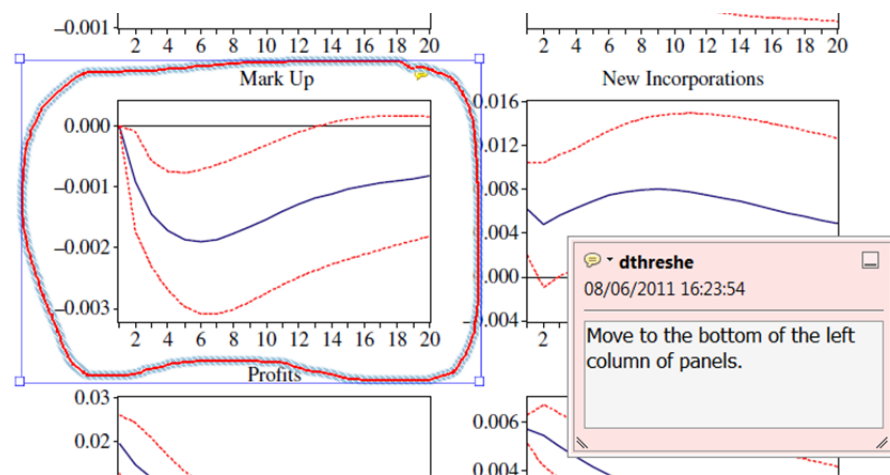
For further information on how to annotate proofs, click on the Help menu to reveal a list of further options:

WILEY-BLACKWELL
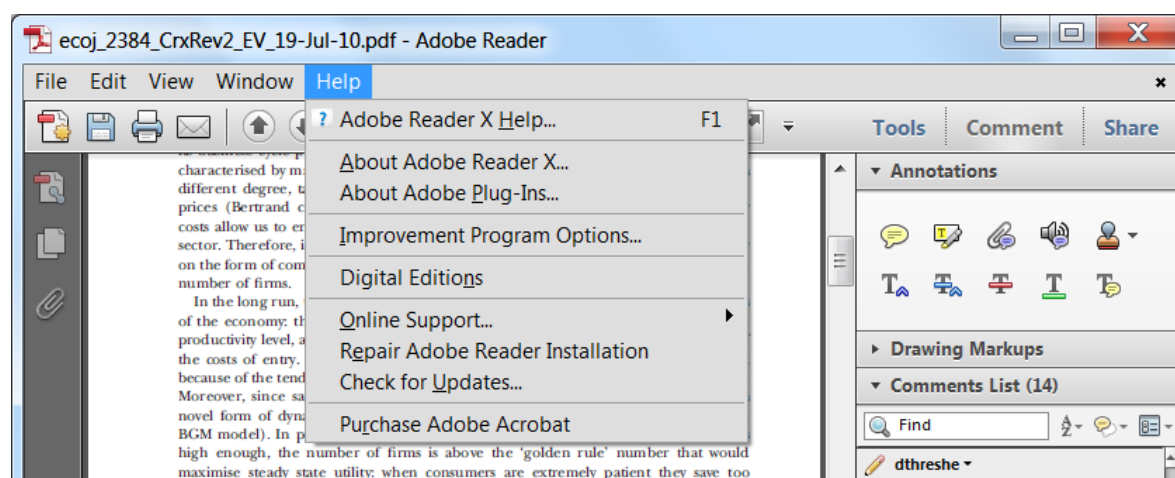
Additional reprint and journal issue purchases

Should you wish to purchase additional copies of your article,
 please click on the link and follow the instructions provided:
 https://caesar.sheridan.com/reprints/redir.php?pub=10089&acro=GRL

Corresponding authors are invited to inform their co-authors of
the reprint options available.

Please note that regardless of the form in which they are acquired,
reprints should not be resold, nor further disseminated in electronic form, nor
deployed in part or in whole in any marketing, promotional or educational
contexts without authorization from Wiley. Permissions requests should be
directed to mailto: permissionsus@wiley.com

For information about 'Pay-Per-View and Article Select' click on the following
link: http://wileyonlinelibrary.com/ppv